processes

MDPI

Article

In Situ Synthesis of Zero-Valent Iron-Decorated Lignite Carbon for Aqueous Heavy Metal Remediation

Hasara Samaraweera [1,2], Samadhi Nawalage [1], R. M. Oshani Nayanathara [3], Chathuri Peiris [1], Tharindu N. Karunaratne [3], Sameera R. Gunatilake [2], Rooban V. K. G. Thirumalai [4], Jilei Zhang [3], Xuefeng Zhang [3,*] and Todd Mlsna [1,*]

[1] Department of Chemistry, Mississippi State University, Mississippi State, MS 39762, USA
[2] College of Chemical Sciences, Institute of Chemistry Ceylon, Rajagiriya 10107, Sri Lanka
[3] Department of Sustainable Bioproducts, Mississippi State University, Mississippi State, MS 39762, USA
[4] Institute for Imaging and Analytical Technologies, Mississippi State University, Mississippi State, MS 39762, USA
* Correspondence: xz210@msstate.edu (X.Z.); tmlsna@chemistry.msstate.edu (T.M.)

Abstract: Lignite's large abundance, physicochemical properties and low cost are attractive for industrial wastewater remediation. However, directly applying lignite for wastewater treatment suffers low efficiency. Here, we synthesize highly efficient zero-valent iron (ZVI)-decorated lignite carbon through the in-situ carbonization of a lignite and $FeCl_2$ mixture for heavy metal removal. The effect of carbonization temperature on the morphology, structure and crystallite phases of ZVI-decorated lignite carbons (ZVI-LXs) was investigated. At an optimized temperature (i.e., 1000 °C), ZVI particles were found evenly distributed on the lignite matrix with the particles between 20 to 190 nm. Moreover, ZVI particles were protected by a graphene shell that was formed in situ during the carbonization. The synthesized ZVI-L1000 exhibited higher Cu^{2+}, Pb^{2+} and Cd^{2+} stripping capacities than pristine lignite in a wide pH range of 2.2–6.3 due to the surface-deposited ZVI particles. The maximum Langmuir adsorption capacities of ZVI-L1000 for Cd^{2+}, Pb^{2+} and Cu^{2+} were 38.3, 55.2 and 42.5 mg/g at 25 °C, respectively, which were 7.8, 4.5 and 10.6 times greater than that of pristine lignite, respectively. ZVI-L1000 also exhibited a fast metal removal speed (~15 min), which is ideal for industrial wastewater treatment. The pseudo-second-order model fits well with all three adsorptions, indicating that chemical forces control their rate-limiting adsorption steps. The reduction mechanisms of ZVI-L1000 for heavy metals include reduction, precipitation and complexation.

Keywords: lignite; ZVI; carbothermal reduction; in situ synthesis; heavy metal removal

check for updates

Citation: Samaraweera, H.; Nawalage, S.; Nayanathara, R.M.O.; Peiris, C.; Karunaratne, T.N.; Gunatilake, S.R.; Thirumalai, R.V.K.G.; Zhang, J.; Zhang, X.; Mlsna, T. In Situ Synthesis of Zero-Valent Iron-Decorated Lignite Carbon for Aqueous Heavy Metal Remediation. *Processes* **2022**, *10*, 1659. https://doi.org/10.3390/pr10081659

Academic Editor: Guining Lu

Received: 16 July 2022
Accepted: 18 August 2022
Published: 21 August 2022

1. Introduction

Rapid industrialization and population growth have accelerated environmental pollution worldwide. Approximately 7 million tons of wastewater are discharged into surface water annually, which has caused a severe clean water crisis [1]. In particular, heavy metals (HMs) are considered the most noxious inorganic aquatic contaminants because they are bioaccumulative, non-biodegradable and persistent [2]. Copper and cadmium are categorized as priority pollutants because of their high frequency of occurrence in HM effluents [3]. Large HM production stimulates the great discharge of HM, causing build-up in the environment [4] and stimulating adverse health disorders such as liver and kidney failure, mucosal irritations, lung cancers, chronic headaches, anemia, diarrhea and damage to the reproductive system [5]. Conventional water remediation strategies such as precipitation, ion exchange, membrane process, electrodeposition and adsorption are employed for HM removal from groundwater [6]. However, in situ remediation offers massive cost savings over groundwater treatment.

Zero-valent iron (ZVI) is an environmentally benign material with strong reducing power and high reactant activity for environmental remediation [7]. Usually, small-sized

ZVI particles (i.e., nanosized or few-micrometer-sized) are desired because their small particle size and high surface area ensure good reactivities towards contaminants [8,9]. In particular, nanoscale ZVIs (nZVIs) offer both outstanding adsorption and catalytic abilities, and their use has been pronounced for pollution control over the past two decades. However, owing to their high surface energy, ferromagnetic properties and high reactivity, small-sized ZVI particles (especially nZVI) suffer aggregation and rapid passivation issues [10,11], which lead to colloidal instability and rapid reactivity loss. Incorporating nanomaterials (i.e., nZVI) into the adsorbents can improve pollutant removal efficiencies since both the pristine adsorbent and the nanophase act as the adsorbents. On the other hand, the use of cost-effective nanomaterials has been highlighted in recent industrial applications on a global and regional scale. Carbon-supported ZVI sorbents have been recently developed to reduce ZVI agglomeration and provide long-term stability [12,13]. Nevertheless, ZVI-biochar hybrids are highly effective at contaminated soil and water remediation due to the presence of quinone and graphene, enhancing electron transfer towards pollutants [14]. ZVI-carbon hybrids remove HMs in many pathways (e.g., direct reduction, surface adsorption followed reduction, surface complexation and coprecipitation), as the removal is performed by both the carbon source and the ZVI. Generally, ZVI-biochar hybrids are produced from the borohydride (BH_4^-) reduction route, where biochar particles are dispersed in an aqueous solution containing Fe^{2+} and/or Fe^{3+} ions, followed by BH_4^- addition to convert $Fe^{2+/3+}$ ions to ZVI that attach onto biochar surfaces [8]. However, the toxicity and high cost of borohydrides make this approach less appealing for large-scale production and broad applications. Recently, the in-situ synthesis of ZVI-biochar hybrids through the carbothermal reduction approach has received more and more attention because of its easy synthesis, low cost and scalability [9].

Recent studies have discovered that lignite can also be modified like pristine biochar to improve surface properties with enhanced adsorption features [15–18]. Lignite's immediate availability, plenty of minerals and affordability improve its potential practical applications. It is an important carbon source like biochar; therefore, it can be used for supporting metal (hydro-)oxides and Fe^0 through surface coprecipitation or deposition [17]. Previously studies have used lignite to strip phosphate, nitrate, dyes and heavy metals from aqueous media [16,17,19,20]. No previous investigations have been conducted to design ZVI-decorated lignite carbon through the carbothermal reduction approach for water treatment until now.

In this work, the in-situ synthesis of ZVI-decorated lignite carbon (ZVI-LX) was carried out using the carbothermal reduction of $FeCl_2$ using lignite at different temperatures (600–1000 °C). It was found that prepared ZVI-LXs exhibited temperature-dependent ZVI accumulation and metal ion removal abilities. At 1000 °C, the as-synthesized ZVI-L1000 displayed a distinct structure and morphology compared to ZVI-LXs synthesized at 600–900 °C. Crystalline phases formed in ZVI-L1000 were determined using XRD analysis. Surface elemental percentages and functional groups were acquired using SEM-EDX and FTIR analysis. SEM observations showed that nZVI particles were dominating on the lignite carbon surface, and few-micrometer-sized ZVI particles were also observed. TEM analysis revealed that the nZVI particles were encapsulated by graphitic carbon layers. Furthermore, the heavy metal (Cu^{2+}, Pb^{2+} and Cd^{2+}) removal capacity of ZVI-L1000 was evaluated.

2. Materials and Methods

2.1. Materials

Lignite was supplied from North American Coal Company (Ackerman, MS, USA). This sample was dried and sieved to a particle size of 150–250 μm before use. Analytical grade $Pb(NO_3)_2$, $Cd(NO_3)_2$, $Cu(NO_3)_2$ and $FeCl_2{\cdot}4H_2O$ were purchased from Sigma Aldrich (St. Louis, MO, USA). Lignite contains C, O, Al and Si as principle elements [17].

2.2. Development of ZVI-Decorated Lignite Carbon through Carbothermal Reduction

Lignite (18.0 g) and $FeCl_2 \cdot 4H_2O$ (8.64 g) were weighed and transferred to a 250 mL beaker (this mixture contained 10 wt.% Fe). Acetone and DI water (15 mL each) were added to the beaker to dissolve $FeCl_2$. This suspension was heated on a hot plate at (~300 °C) for 30 min to evaporate the solvents. During the heating, Cl_2 gas bubbles were released, and the beaker was covered with a watch glass to avoid solvent splashing. After that, the solid residue (Fe^{2+} impregnated lignite) was oven-dried at 110 °C overnight. The carbothermal reduction was initiated by carbonized Fe^{2+}-impregnated lignite in an electric tubular furnace. Briefly, approximately 20 g of dried solid was loaded into two ceramic boats and inserted into the furnace, followed by heating the furnace to the predetermined temperature (i.e., 600, 700, 800, 900 or 1000 °C) with a ramping rate of 50 °C/min. After holding the temperature for 1 h, the furnace was turned off and naturally cooled down to room temperature. Nitrogen gas (99.999% purity, 1 L/min) was purged into the tubular furnace during the carbonization and cooling processes. The carbonization products, namely ZVI-LX, where X refers to the carbonization temperature, were stored in plastic bottles before the characterization and adsorption experiments. Approximately 15 g of the ZVI-LX products was obtained for all carbothermal reduction experiments, and the corresponding ZVI-LX yields were ~75%.

2.3. Analytical Methods and Characterization

The structure and morphology of ZVI-LX were characterized using scanning electron microscopy (SEM, JEOL JSM-6500F) and transmission electron microscopy (TEM, JEOL 2100). The surface elemental composition of ZVI-LXs was characterized using SEM-EDX. The iron crystalline structure and phase composition in ZVI-LXs were identified using the Rigaku ultima III XRD diffractometer (20–80° with 2°/min and step size 0.05°). The thermogravimetric analysis (TGA) of lignite and ZVI-L1000 was conducted using a thermogravimetric analyzer (TA Instruments Q50) under N_2. Functional groups present on lignite, Fe^{2+}-impregnated lignite and ZVI-L1000 were characterized using Fourier-transform infrared spectroscopy (PerkinElmer FTIR spectrometer). The complete acid digestion of ZVI-L1000 vs. lignite followed by AAS was performed to determine the total iron content. The ash content and moisture content of ZVI-L1000 vs. lignite were found using ASTM D2974-14. A series of pH-adjusted NaCl solutions were used to determine the adsorbent point of zero charge (PZC).

2.4. Batch Sorption Experiments

Heavy metal uptake experiments were conducted by dispersing 50 mg sorbent (i.e., lignite and ZVI-LX) into 25 mL metal ion solutions in plastic centrifuge vials and by shaking (200 rpm). The initial pH of Cu^{2+}, Pb^{2+} and Cd^{2+} ionic solutions was changed from 2.2 to 6.4, and the equilibrium pH was reported after each experiment. The heavy metal uptake kinetics experiments were conducted starting from 5 min to 1 h. The heavy metal uptake isotherm experiments were conducted at 25 °C, respectively, with a contact time of 15 min and an initial metal ion concentration ranging from 25 to 400 ppm. The simultaneous removal of Cu^{2+}, Pb^{2+} and Cd^{2+} was also investigated (25 mL of 1000 ppm cation concentration in each and 0.5 g of adsorbent, 25 °C, pH 5.8). Replicates and controls were utilized in each adsorption experiment. Residual metal ion concentrations in supernatant solutions were determined using an atomic absorption spectrophotometer (AAS).

Metal ion uptake capacity (mg/g) can be calculated using

$$\text{Uptake capacity}\left(q_e\right) = \frac{(C_i - C_f)V}{m}$$

Metal ion removal efficiency (%) can be found with

$$\%\text{Cu(II) removal} = \frac{(C_i - C_f) \times 100}{C_i}$$

where C_e= equilibrium metal ion concentration (mg/L), C_i = initial metal ion concentration (mg/L), C_f = final metal ion concentration (mg/L), V = volume of the solution (L) and m = mass of the adsorbent (g).

Uptake kinetics were evaluated using pseudo-first and -second-order kinetic models, and uptake isotherm data were evaluated using Langmuir and Freundlich isotherm models (Table 1).

Table 1. Kinetic and isotherm models with nonlinear and linear forms.

Kinetic Model	Nonlinear Form	Linear Form
Pseudo-first-order	$q_t = q_e\left(1 - e^{-kt}\right)$	$\log(q_e - q_t) = \log(q_e) - \frac{k_1 t}{2.303}$
Pseudo-second-order	$q_t = \frac{k_2 q_e^2 t}{1+k_2 q_e t}$	$\frac{t}{q_t} = \frac{1}{k_2 q_e{}^2} + \frac{t}{q_e}$
Langmuir isotherm	$q_e = \frac{q_m K_L C_e}{1+K_L C_e}$	$\frac{C_e}{q_e} = \frac{C_e}{q_m} + \frac{1}{q_m K_L}$
Freundlich isotherm	$q_e = K_f C_e{}^{1/n}$	$\ln q_e = \ln K_f + \frac{1}{n} \ln C_e$

where, q_e and q_t (mg/g) are the metal ion uptake capacity at the equilibrium time and at the given time, t, respectively; C_e (mg/L) is the equilibrium concentration; K_L (L/mg) and K_f are the constants; q_m (mg/g) denotes the maximum uptake capacity; and *1/n* is the heterogeneity factor. Origin 2021b software was used to draw XRD spectra and batch plots. ChemDraw Ultra 13.0 was used to draw the structures and the graphical image.

3. Results

3.1. Structure, Morphology and Heavy Metal Uptake Performance of ZVI-LX Particles

The FTIR spectra of ZVI-LXs and lignite were scanned from 500–4500 cm^{-1} (Figure 1a). Lignite is carbon-rich organic matter that consists of many functional groups, including alkyl branches (C-H stretching at 2917 and 2922 cm^{-1}, C-H bending vibrations at 1428 cm^{-1}), aromatic rings (C=C stretching at 1605 cm^{-1}), hydroxyls (O-H vibrations at 3620 cm^{-1}), carbonyls (C=O at 1650 cm^{-1}, this peak is overlapped with the C=C peak), Si-O-Si, Si-O-C (1031 and 1010 cm^{-1}), C-H out-of-plane vibrations of aromatic ring structures (745 cm^{-1}), aromatic ether oxygen bond stretching vibrations of alcohols, phenols and acids (1263 cm^{-1}), ether oxygen bonds (1117 cm^{-1}) [21] as well as clay and silicate minerals (544 cm^{-1}) [22], as depicted by the FTIR spectrum. After $FeCl_2$ impregnation, the peak related to C=O groups at 1650 cm^{-1} shifted to 1707 cm^{-1}, indicating Fe^{2+} physisorption under Van der Waals forces [23]. Furthermore, the peaks related to C-O stretching at 1263 and 1117 cm^{-1} were reduced and indicate the Fe^{3+} interactions with oxygen-containing functional groups in lignite [12]. Moreover, peaks centered at 636 cm^{-1} and 630 cm^{-1} were also observed, which are related to Fe-O-C [24,25]. After carbonizing the $FeCl_2$/lignite mixture at 600 °C, the peak at 636 cm^{-1} shifted to 635 cm^{-1}, and the peak intensity also increased (Supplementary Materials, Figure S1). This indicates that the impregnated Fe^{2+} reacted with oxygen-containing functionalities in the lignite and formed Fe_2O_3 particles [26]. However, further increasing the temperature from 700 to 900 °C caused a reduction in Fe-O peak intensity, suggesting the reduction of Fe_2O_3 to Fe^0. At 1000 °C the disappearance of the Fe-O peak indicated the complete reduction of Fe_2O_3 to Fe^0.

XRD patterns of lignite and ZVI-LXs are shown in Figure 1b. Lignite has a broad crystalline peak at 2θ = 24.9°, indicating that it is mainly composed of amorphous carbon. Furthermore, peaks located at 2θ = 20.8° and 26.6° correspond to the (100) and (011) reflections of quartz (SiO_2) that are overlapped with the amorphous carbon peak [17]. After Fe^{2+} impregnation and carbonization at 600 °C, the synthesized ZVI-L600 showed Fe_2O_3 and SiO_2 diffraction peaks, indicating the thermal decomposition of $FeCl_2$ to Fe_2O_3 in the presence of lignite (Figure 1b). ZVI-L700 shows a distinct XRD pattern compared to ZVI-L600, in which the dominating metallic body-centered cubic iron (α-Fe) diffraction peaks (2θ = 44.6° and 65.2°) are observed [27], along with a weak Fe_2O_3 peak at 2θ = 35.4° [14]. These observations indicate that the carbothermal reduction of $FeCl_2$ to nZVI by lignite requires 700 °C, which is different from the carbothermal reduction of $Fe(NO_3)_3$ by lignin, which requires 600 °C [28]. At carbonization temperatures above 800 °C, the α-Fe peaks still dominate, whereas the Fe_2O_3 peak becomes invisible, and a weak metallic face-centered cu-

bic iron (γ-Fe) at 43.6° is observed [29]. γ-Fe is an unstable iron phase below the iron–carbon eutectic temperature (727 °C) at room temperature [30]. The presence of γ-Fe nanoparticles in the ZVI-L700 implies that they are confined in graphene shells [14,29,31–33]. Furthermore, an increase in the carbonization temperature to 1000 °C leads to a reduction in the α-Fe diffraction intensity and an increase in γ-Fe diffraction intensity, along with a visible and broad carbon (002) diffraction peak. These results indicate that higher temperatures facilitate the conversion of α-Fe to γ-Fe along with the formation of more graphene shells through carbon dissolution and precipitation [14].

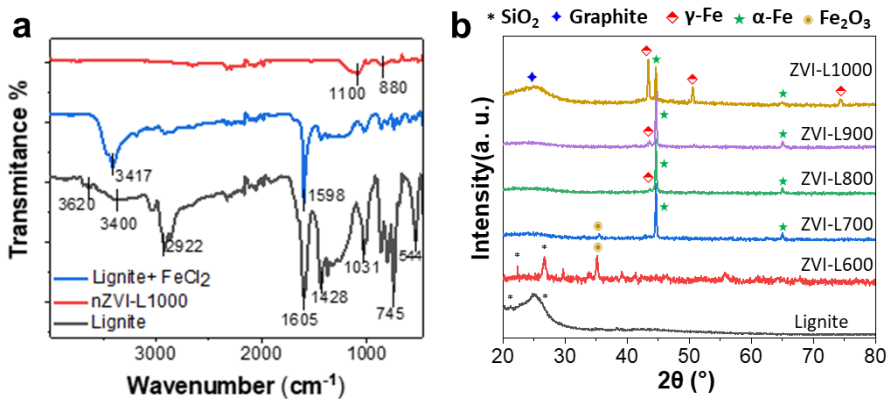

Figure 1. (**a**) Baseline-corrected FTIR spectra of lignite, $FeCl_2$-impregnated lignite and ZVI-L1000; (**b**) XRD patterns for ZVI-LXs synthesized at 600–1000 vs. lignite.

ZVI-LX synthesis conditions (effect of temperature, salt type and concentration) were optimized to determine the hybrid with the highest Cu^{2+}, Pb^{2+} and Cd^{2+} removal performance at 25 °C (initial metal ion concentration, 100 ppm, solution volume, 25 mL, 24 h, pH 5.5). The uptake capacities of ZVI-LXs synthesized at different temperatures (600–1000 °C) and the lignite are shown in Figure 2**.** The uptake capacities of lignite towards Cd^{2+}, Cu^{2+} and Pb^{2+} are 7.4, 2.9 and 10.4 mg/g, respectively at pH 5.5. ZVI-L600 exhibited lower capacities, i.e., Cd^{2+} 4.6 mg/g, Cu^{2+} 1.3 mg/g and Pb^{2+} 6.7 mg/g, in comparison with lignite. This is because $FeCl_2$ was not reduced to ZVI at 600 °C, as illustrated by the XRD pattern Error! Reference source not found. With the increasing carbonization temperature of ZVI-LX, the removal capacities of all three metals were improved (Figure 2) for the results of the reduction of $FeCl_2/Fe_2O_3$ to ZVI (more details are in FTIR and XRD analyses). In particular, ZVI-L1000 showed the greatest affinity towards Cd^{2+}, Cu^{2+} and Pb^{2+}, with uptake capacities of 11.4 mg/g, 31.1 mg/g and 23.1 mg/g, respectively.

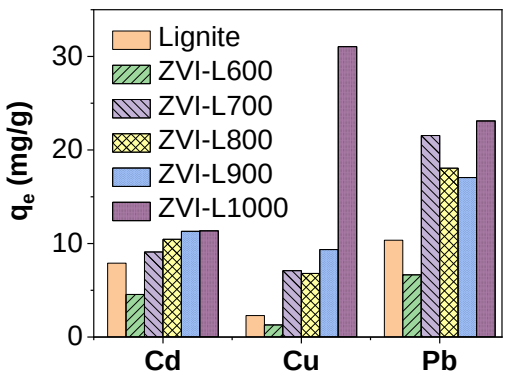

Figure 2. Comparison of heavy metal uptake capacities of lignite and ZVI-LX synthesized at 600–1000 °C.

TGA profiles were obtained for both lignite and $FeCl_2$-impregnated lignite under nitrogen (Figure S2). Lignite showed very little mass loss at the early stages of the temperature ramping (<200 °C), whereas a significant weight loss was observed at a temperature

between 400 and 600 °C, corresponding to the thermal degradation of its surface functional groups. Moreover, mass loss at temperatures above 600 °C was attributed to the carbonization of lignite. In comparison with lignite, $FeCl_2$-impregnated lignite showed huge mass loss at a temperature below 200 °C, indicating the presence of $FeCl_2$ salt promoting the lignite thermal degradation. Another significant weight loss observed at a temperature above 700–1000 °C corresponded to the reduction of $FeCl_2$ to ZVI. The total mass losses for lignite and ZVI-L1000 were 16.5% and 6.7%, indicating that ZVI-L1000 restricted huge mass losses due to its high inorganic ash (e.g., iron) content.

To investigate why ZVI-L1000 outperformed ZVI-L700, ZVI-L800 and ZVI-L900 for heavy metal uptake, despite all the samples showing dominated metallic iron diffraction peaks by XRD (Figure 2), SEM characterizations were conducted for ZVI-LXs obtained at 700–1000 °C (Figure 3a–d). The lignite surface (Figure 3a) was smooth and contained a few tiny and large SiO_2 crystallites [17]. After impregnation using Fe^{2+} followed by carbonization, ZVI-LX samples showed rough surfaces with many iron nanoparticles, which was in agreement with previous studies [34]. Moreover, some few-micrometer-sized ZVI particles (1–2 μm) were also observed (Figure 3e,f), which were generated from the aggregation and merging of nZVI particles at evaluated temperatures. With the increase in carbonization temperature, the particle shape changed from irregular (indicating iron oxides and other iron compounds, possibly $FeCl_2$ or FeS) to spherical (indicating ZVI). The SEM-EDX analysis of ZVI-L700 and ZVI-L1000 is displayed in Figure 3e,f, respectively, and the corresponding elemental percentages are shown in Figure S4. The mapping results show that ZVI-L700 (Figure 3e) contained both iron oxides (e.g., Fe_2O_3) and ZVI, whereas ZVI-L1000 (Figure 3f) barely contained Fe oxides. ZVI-L700 contained a higher atomic O percentage than ZVI-L1000 (8.8% vs. 0.9%) and a lower Fe percentage (4.6% vs. 23.92%) (Figure S4). Moreover, ZVI-L700 contained more Cl than ZVI-L1000, indicating the presence of $FeCl_2$ residues at 700 °C. These Fe oxides and $FeCl_2$ compounds may have been amorphous or may have had weak crystallinity in comparison with ZVI, which made them invisible by XRD. These observations indicate that a high temperature (i.e., 1000 °C) was necessary to fully convert $FeCl_2$ to ZVI, which is essential for heavy metal removal, and enabled a superior heavy metal uptake capacity of ZVI-L1000.

TEM analysis was conducted for ZVI-L1000 to examine the detailed morphology of nZVI particles (Figure 3g–j). These nZVI particles had a spherical shape with a particle size ranging from 20 nm to 190 nm (Figure 3g). The typical chain-like structure of nZVI [35] was invisible due to the lignite supporter helping in reducing the chemical and magnetic attraction between nZVIs providing a good dispersion. Furthermore, it showed dark patches of mass concentrated areas of nZVI grains encapsulated with a graphitic phase grown from lignite. Evidence for graphitic carbons in lignite is provided by both XRD and d-spacing determination. At a higher resolution, the core–shell structures of nZVIs are quite visible (Figure 3h), dispersed on graphene sheets which could enhance the stability of nZVI preventing their aggregation. As in Figure 3i, the graphene shell is not perfect and has some defects, and these defects slow down electron transfer, resulting in nZVIs' long-term usage [36]. The d_{002} spacing of ZVI-L1000, 0.34 nm, (Figure 3j) corresponds to graphitic carbon's 002 lattice space [37].

The PZC of ZVI-L1000 (6.9) was greater than that of the raw lignite (3.9) [17], indicating that deposited ZVI affected the surface charge of the hybrid and enabled more positive surface formation. When exposed to water, both iron oxides/hydroxides could be formed on ZVI-L1000 because of the oxidation of Fe^0. These oxides/hydroxides had local PZCs ranging from 6 to 9.2 (i.e., α-Fe_2O_3 = 6.8–9.2, $Fe_3O_4 \approx 7.8$, α-FeOOH = 9, γ-Fe_2O_3 = 6.3), resulting in a higher PZC of ZVI-L1000 than lignite [38]. This high PZC could facilitate stormwater treatment (pH 6.2–7.2) via electrostatic bonding and complexation.

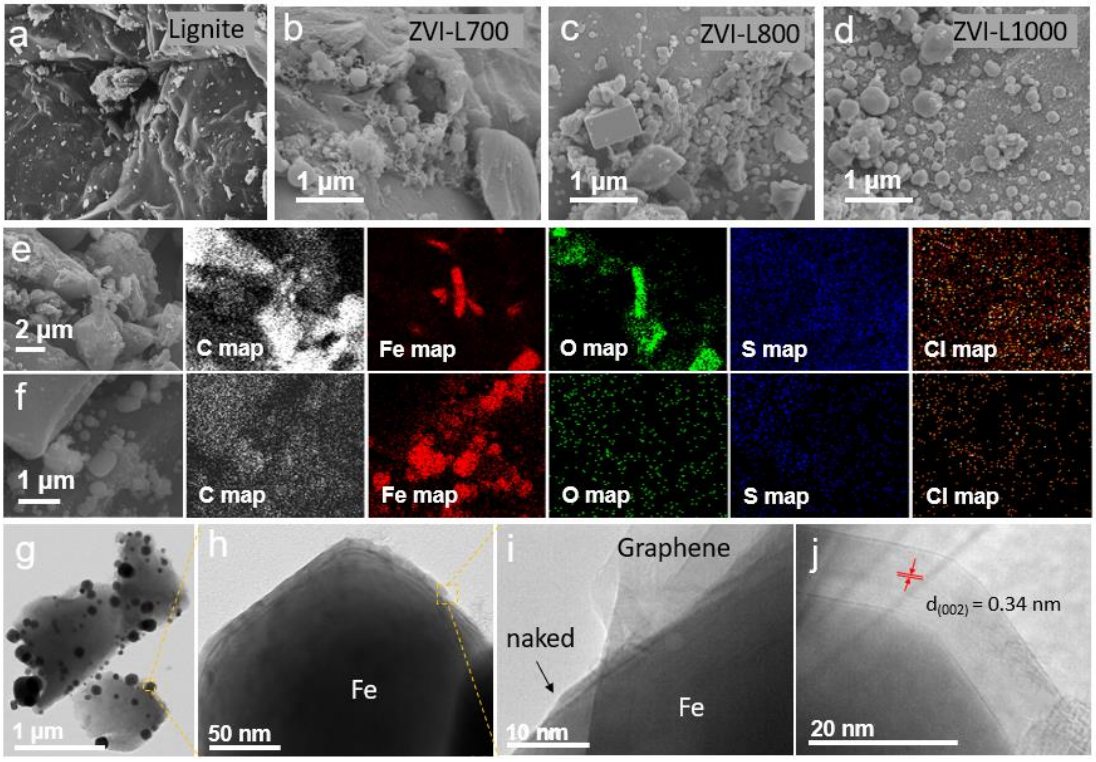

Figure 3. (**a**–**d**) SEM images of lignite and ZVI-LXs synthesized at 700, 800 and 1000 °C; (**e**,**f**) SEM images and their corresponding EDX mapping spectra of ZVI-L700 (**e**) and ZVI-L1000 (**f**); (**g**–**j**) TEM micrographs of ZVI-L1000 showing the distribution of nZVI (dark spheres) in lignite carbon (irregular shaped light color matrix) (**g**), nZVI particle composed of a graphene encapsulation and a metallic iron core (**h**), the imperfect graphene shell with some defects (**i**), the determination of d-spacing of graphene layers (**j**).

It is worth noting that $Fe(NO_3)_3$ (with 28% Fe loading) and $FeCl_2$ (with 28% 15% Fe loadings) have also been used to prepare three different ZVI-L1000s, and the metal binding capacities of the products were evaluated (25 mL metal solution, 0.05 g dose, pH 5, 25 °C). All three hybrids exhibited higher metal ion removals than lignite due to iron modification (data are not presented). Interestingly, the greatest metal uptake capacity was achieved by the $FeCl_2$-derived ZVI-L1000 with 28% Fe loading, which indicates that the removal of heavy metal ions is both iron salt ($FeCl_2$ outperformed $FeNO_3$) and iron loading (28% Fe outperformed 15% and 10% Fe) dependent. Despite the $FeCl_2$ with 28% Fe outperforming 10% Fe, too much iron was used in the former one, which may make the overall ZVI-L1000 production process cost-ineffective. Therefore, $FeCl_2$ with 10% Fe loading was selected for nZVI-1000 production and was used for the following heavy metal removal experiments.

3.2. pH Dependence and the Kinetics of Heavy Metal Removal

Considering that heavy metal ions precipitate from the solution at neutral and alkaline pH conditions, the pH studies were conducted between pH 2.2 and 6.4 to avoid a decrease in soluble metal ion concentrations by precipitation. As in Figure 4a–c, the pH-dependent metal removals were observed for ZVI-L1000 from pH 2.2 to 6.4 (initial metal ion concentration, 100 ppm, solution volume, 25 mL, 15 min, 25 °C). ZVI-L1000 (PZC = 6.9) showed low Cd^{2+}, Cu^{2+} and Pb^{2+} adsorption capacities (0.5, 0.4, and 6.8 mg/g) at acidic pH levels, i.e., pH 2.2. When increasing the initial solution pH to ~6, the uptake capacities of all three cations were significantly enhanced by 20, 15 and 3 times for Cd^{2+}, Cu^{2+} and Pb^{2+}, respectively.

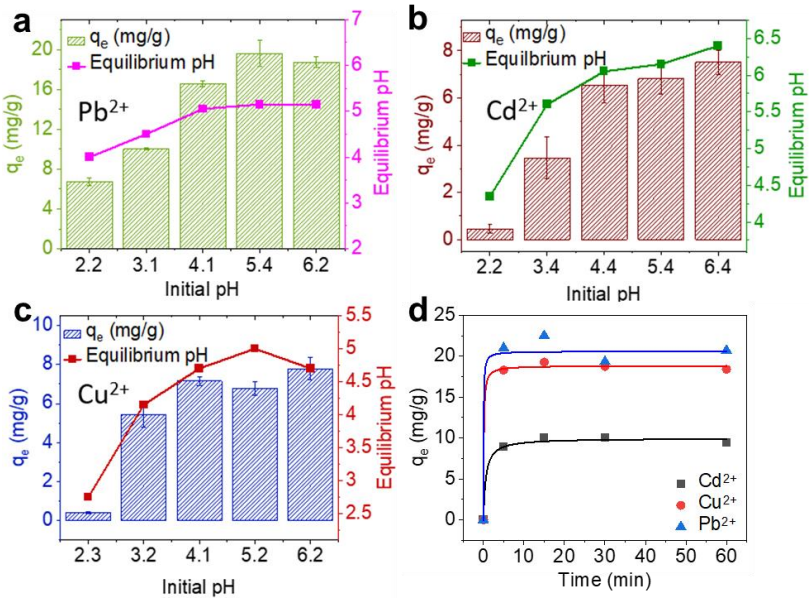

Figure 4. (**a**–**c**) pH dependence on (**a**) Pb^{2+}, (**b**) Cd^{2+} and (**c**) Cu^{2+} uptake by ZVI-L1000 (initial concentration 100 ppm, solution volume 25 mL, 25 °C, 15 min); (**d**) Pseudo-second-order kinetic fittings for Cu^{2+}, Pb^{2+} and Cd^{2+} uptake by ZVI-L1000 (initial concentration 100 ppm, solution volume 25 mL, 25 °C, pH values 6.4 (Cd^{2+}), 6.2 (Cu^{2+}) and 5.4 (Pb^{2+})).

Pb^{2+} uptake increases when the solution pH increases from pH 2.2 to 5.4 (Figure 4a), and further increasing the solution pH does not improve the Pb^{2+} removal capacity. Considering that ZVI particles (Fe^0, −0.44 V) have a lower reduction potential than lead (Pb^0, −0.13 eV), the Pb^{2+} uptake by ZVI-L1000 is mainly caused by the single-displacement reaction between ZVI and Pb^{2+} ($Fe^0 + Pb^{2+} \rightarrow Fe^{2+} + Pb^0$). At low pH range, ZVI particles in the ZVI-L1000 surface are consumed by H^+ through the following reaction: $Fe^0 + 2H^+ \rightarrow Fe^{2+} + H_2$ [14, 39]. This is evidenced by the immediate formation of bubbles after adding ZVI-L1000 into the Pb^{2+} solution along with the increase in the solution pH after Pb^{2+} removal (Figure 4a). Therefore, the increase in solution pH results in higher Pb^{2+} capacity. Moreover, the formation of iron oxides/hydroxides [e.g., FeOOH, $Fe(OH)_2$ and $Fe(OH)_3$] in aqueous solutions exhibits more negative sites (e.g., Fe-O^-, pK_a 5.6) at a higher pH, and this also contributes to increased Pb^{2+} capacity. Tang et al. (2020) observed a formation of different Pb phases (i.e., Pb^0, PbO, PbO_2) after Pb^{2+} uptake, suggesting that Pb^{2+} removal via adsorption and precipitation is kinetically favored as well [36]. PbO and PbO_2 were deposited on the adsorbent surface via the oxidation of Fe^{3+} phases (Fe^{3+} oxides, hydroxides and oxide-hydroxides.) on ZVI. Du et al. (2019) also reported the formation of $Pb(OH)_2$ and $PbCO_3$ due to −OH abstraction from water and CO_2 dissolved in water [39]. As Fe^{3+} hydroxides are formed when ZVI-L1000 is added to the Pb^{2+} solution, the above-mentioned insoluble Pb precipitates could also be formed in this study.

Cadmium ions are unlikely to hydrolyze at an initial pH < 8 [40] and tend to exist as divalent species during the studied pH levels. Therefore, ZVI-L1000 (PZC = 6.9) is suitable for the Cd^{2+}-contaminated stormwater (pH 7) treatment. Similar to Pb^{2+} removal, ZVI particles in the ZVI-L1000 can reduce Cd^{2+} because of the higher reduction of Cd (0.40 eV) [41]. Therefore, a higher solution pH avoids the leaching of nZVI by H^+ and thereby increases the updated capacity of Cd^{2+} through reduction. Moreover, the oxidation products such as iron oxides/hydroxides can bind with Cd^{2+}/$Cd(OH)^+$ via electrostatic bonding/complexation, improving cadmium ion removal (Figure 4b).

Similar to Pb^{2+}, Cu^{2+} can be reduced to Cu^0 and Cu^+ by ZVI particles in the ZVI-L1000 [42,43]. Therefore, lower Cu^{2+} uptake at a more acidic pH is also attributed to the consumption of ZVI by H^+. Moreover, the oxidation products of ZVI with basic Fe-O^-

surface sites are formed in the solution, favoring the adsorption of $Cu^{2+}/Cu(OH)^{+}$ at a higher pH (Figure 4c).

The time required to reach equilibrium determined the practical value of the adsorbent. The removal of heavy metals was rapid, with approximately 18% Cd^{2+}, 50% Cu^{2+} and 50% Pb^{2+} of the ultimate uptake completed within 5 min (Figure 4). When the contact time increased, the uptake of the three metal ions rose until 15 min. Therefore, 15 min was selected as the equilibrium time for the isotherm experiments. Several factors affected the rate of metal ion removal by ZVIs. The low Fe:lignite impregnation ratio (1:10) improved both the access to metal ions and the removal rate, overcoming the steric hindrance caused by nano Fe^{0}. The removals decreased after 15 min, which could be due to a supersaturation state. At this time, desorption predominated over adsorption [44]. The kinetic data were fitted using pseudo-first and -second-order kinetic models. The pseudo-second-order kinetic model (R^2 = 0.997–0.999) fits better than pseudo-first-order kinetic model (R^2 = 0.997–0.999) (Table S1), suggesting that chemisorption could be the rate-limiting step. The q_e (calc.) values of Cd^{2+} (10.4 mg/g), Cu^{2+} (20.4 mg/g) and Pb^{2+} (21.5 mg/g) in the pseudo-second-order kinetic model are close to their experimental values (10.2, 19.3, and 22.5 mg/g, respectively). The K_2 value of Cd^{2+} (0.16 min^{-1}) is the greatest, whereas 0.07 min^{-1} and 0.12 min^{-1} were the values for Cu^{2+} and Pb^{2+} (Table S1).

3.3. Adsorption Isotherm

The adsorption isotherms of Cu^{2+}, Pb^{2+} and Cd^{2+} adsorption by ZVI-L1000 and lignite were performed at 25 °C (Figure 4d) using 25–400 ppm metal ion solutions. Both Langmuir (R^2 = 0.97–0.99) and Freundlich isotherm (R^2 = 0.92–0.99) models were consistent with all adsorptions. Cu^{2+}, Pb^{2+} and Cd^{2+} adsorption capacities of ZVI-L1000 (42.5, 55.2, and 38.3 mg/g) were greater than lignite (4.0, 12.2 and 4.9 mg/g) due to the existence of ZVI (Table 2). The metal adsorption capacity of ZVI-L1000 decreased according to the order: $Pb^{2+} > Cu^{2+} > Cd^{2+}$ at 25 °C. Differences in hydrated ionic radii, standard reduction potential, and the electronegativity of metal ions affected the cation removals. Standard reduction potentials decreased according to this order: $Cu^{2+}/Cu(s)$ (0.34 V) > $Pb^{2+}/Pb(s)$ (−0.13 V) > $Cd^{2+}/Cd(s)$ (−0.40 V) > $Fe^{2+}/Fe^{0}(s)$ (−0.41 V). One reason for this could be that positive and slightly positive ions such as Pb^{2+} and Cu^{2+} have large reducing abilities compared to the more negative Cd^{2+} (−0.40 eV). Other reasons could be the differences in hydrated ionic radii and the hydration energy of metal ions. During the adsorption, the hydrated sphere surrounding the cation should be dissociated (spontaneous and entropy-driven), and a cation with a lower hydration energy adsorbs easily via electrostatic interactions. The hydration energy increased as follows: Pb^{2+}(−1481 kJ/mol), Cd^{2+} (−1807 kJ/mol) and Cu^{2+} (−2100 kJ/mol), and the low-energy Pb^{2+} bound to Fe-O^{-} sites in ZVI-L1000 easily [45,46]. Nieva et el. (2017) reported a large Pb^{2+} affinity towards ZVI due to the less negative standard reduction potential of $Pb^{2+}/Pb(s)$ (−0.13 V), a high hydrated ionic radius (0.26 nm), a paramagnetic and large atomic weight (207.2 g/mol) and a high electronegativity (2.33) [42]. Moreover, ZVI-L1000 has a larger affinity towards more electronegative Pb^{2+} (2.33) and Cu^{2+} (1.90) compared to more electropositive Cd^{2+} (1.69) demonstrating that biochar surface area has a minimum effect on Cd^{2+} sorption, but it can be critical in the presence of functional groups.

Table 2. Adsorption isotherm parameters for Cd^{2+}, Pb^{2+} and Cu^{2+} removal by lignite and ZVI-L1000.

Isotherm Model Parameter	Cd^{2+}		Pb^{2+}		Cu^{2+}	
	Lignite	ZVI-L1000	Lignite	ZVI-L1000	Lignite	ZVI-L1000
Langmuir						
q_e (mg/g)	4.9	38.3	12.2	55.2	4.0	42.5
K_L (L/mg)	1.0	0.01	0.07	0.05	1.0	0.07
R^2	0.99	0.99	0.95	0.99	0.99	0.97
Freundlich						
K_F (L/mg)	3.3	3.3	4.0	10.1	1.9	11.0
n	14.5	0.01	4.9	0.3	14.5	3.8
R^2	0.99	0.92	0.99	0.97	0.99	0.99

Note: The heavy metal removal was conducted in the following conditions: 0.05 g adsorbent dose, 25–400 mg/L $Cd^{2+}/Cu^{2+}/Pb^{2+}$ solution, 25 mL solution volume, pH values 6.4 (Cd^{2+}), 5.4 (Pb^{2+}) and 6.2 (Cu^{2+}) at 25 °C, 15 min.

Cd^{2+}, Pb^{2+} and Cu^{2+} adsorption capacities of ZVI-L1000 are comparable with previously developed adsorbents (Table 3). Furthermore, as lignite is an affordable and readily available source material, it offers a greater potential for its commercialization in the future.

3.4. Simultaneous Cu^{2+}, Pb^{2+} and Cd^{2+} Removal by Lignite vs. ZVI-L1000

As shown in Figure S5, both lignite and ZVI-L1000 were used to test the simultaneous removal of Cu^{2+}, Pb^{2+} and Cd^{2+} from aqueous solutions. The ZVI-L1000 showed adsorption selectivity in the following order: $Pb^{2+} > Cd^{2+} > Cu^{2+}$ at pH 5 (400 ppm metal ion concentration, 0.5 g adsorbent dose, 25 °C, 15 min). A similar result has been observed in previous studies as well. Greater adsorption capacities were observed for Pb^{2+}, Cd^{2+} and Cu^{2+} from mono-metal systems (42.5, 55.2, and 38.3 mg/g, respectively) (Figure S5). Comparatively, in multi-metal systems, the adsorption of each metal was greatly suppressed, with Pb^{2+} = 5.5 mg/g, Cd^{2+} = 2.4 mg/g and Cu^{2+} = 0.9 mg/g at pH 5 (400 ppm metal ion, 0.5 g adsorbent dose, 25 °C, 15 min) (Figure S4). This indicates that antagonism is the major competitive effect mechanism here [47]. In this case, all three metal ions compete for a limited number of active sites, decreasing the adsorption. ZVI-L1000 shows a higher Pb^{2+} selectivity due to its lower hydration energy.

The heavy metal removal capacities of ZVI-L1000 are comparable with previously produced adsorbents. Moreover, the carbothermic reduction conducted here is a reduced-cost and eco-friendly method with the use of affordable lignite. This research can be further expanded by using non-biowaste to manufacture ZVI in the future, which would be a significant achievement.

Table 3. Comparison of Cd^{2+}, Pb^{2+} and Cu^{2+} adsorption performance of ZVI-L1000 and lignite with previously developed ZVI adsorbents.

Metal	Material	Fe wt%	Surface Area (m^2/g)	Removal Conditions	Capacity (mg/g)	Ref.
Pb^{2+}	Ostric Bone Ash (OBA)	1.45	67	Pb^{2+} 5–1000 mg/L, 25 °C	88	[13]
Pb^{2+}	OBA-ZVI	18.9	109		160	
Pb^{2+}	Acid ammonium persulfate oxidized corn stalk BC (HPB)	N/A	N/A	Pb^{2+} 50 mg/L, pH 6, 25 °C	135.4	[44]
Pb^{2+}	ZVI-HPB	N/A	N/A	Pb^{2+} 200 mg/L, pH 6, 25 °C	480.9	
Pb^{2+}	Red-mud-supported ZVI	N/A	44.6	Pb^{2+} 100–400 mg/L, pH = 6	149.4	[39]
Cu^{2+}	MWCNT-reinforced ZVI-PAA/PVA polymer mats	N/A	N/A	Cu^{2+} 25–200 mg/L	107.8	[48]
Pb^{2+}	ZVI-L1000	N/A	N/A	25–400 mg/L, pH 6.4 (Cd^{2+}), 6.2 (Cu^{2+}), and 5.4 (Pb^{2+}) 25 °C, 15 min, 25 °C	55.2	This study
Cd^{2+}					38.3	
Cu^{2+}					42.5	

4. Conclusions

The present study reports the novel synthesis of ZVI-decorated lignite carbon through carbothermal reduction to remove Cu^{2+}, Pb^{2+} and Cd^{2+} from aqueous solutions. At 1000 °C, the synthesized ZVI-L1000 showed the highest removal capacities for Cd^{2+} (38.3 mg/g), Pb^{2+} (55.2 mg/g), and Cu^{2+} (42.5 mg/g) at 25 °C. Highly dispersed ZVI particles were responsible for the greater removal performance of ZVI-LXs towards Cu^{2+}, Pb^{2+} and Cd^{2+} uptake compared to lignite. Abundant Fe^0 active centers on the ZVI-L1000 were highly available for metal ion reduction and offered fast removal (~15 min) of all three metal cations compared to recently reported ZVI adsorbents. ZVI-L1000 showed a higher Pb^{2+} selectivity in the presence of Cu^{2+}, Pb^{2+} and Cd^{2+}. Lignite was selected as the carrier here to prepare stabilized ZVI for wastewater treatment. Abundant and low-cost lignite is suitable for the industrial production of value-added products. However, more research is required to identify effective conjugation methods, check the potential applicability of alternative substrates and design better composite platforms aiming to well-disperse the particles and promote their removal performance further. This research can be expanded to evaluate ZVI-L1000's ability to remove organic pollutants, such as pharmaceuticals, pesticides and antibiotics.

Supplementary Materials: The following supporting information can be downloaded at: https://www.mdpi.com/article/10.3390/pr10081659/s1 [49–52].

Author Contributions: Conceptualization, X.Z.; methodology, X.Z.; software, R.V.K.G.T.; validation, X.Z.; formal analysis, H.S.; investigation, H.S.; resources, X.Z. and T.M.; data curation, S.N., R.M.O.N., C.P. and T.N.K.; writing—original draft preparation, H.S.; writing—review and editing, H.S.; supervision, X.Z., T.M. and S.R.G.; project administration, X.Z. and J.Z.; funding acquisition, J.Z. All authors have read and agreed to the published version of the manuscript.

Funding: This research was funded by USDA National Institute of Food and Agriculture (NIFA), Agriculture and Food Research Initiative (AFRI): 2020-65210-30763.

Informed Consent Statement: Not applicable.

Acknowledgments: The authors acknowledge North American Coal Company (Ackerman, MS, USA) for donating lignite for the project. This material is based upon work supported by the National Institute of Food and Agriculture, U.S. Department of Agriculture, under award number 2020-65210-30763. This manuscript is publication #SB1069 of the Sustainable Bioproducts, Mississippi State University (MSU).

Conflicts of Interest: The authors declare no conflict of interest.

References

1. Treto-Suárez, M.A.; Prieto-García, J.O.; Mollineda-Trujillo, Á.; Lamazares, E.; Hidalgo-Rosa, Y.; Mena-Ulecia, K. Kinetic study of removal heavy metal from aqueous solution using the synthetic aluminum silicate. *Sci. Rep.* **2020**, *10*, 10836. [CrossRef] [PubMed]
2. Azimi, A.; Azari, A.; Rezakazemi, M.; Ansarpour, M. Removal of Heavy Metals from Industrial Wastewaters: A Review. *ChemBioEng Rev.* **2017**, *4*, 37–59. [CrossRef]
3. US EPA. 2016. Available online: https://archive.epa.gov/epawaste/hazard/wastemin/web/html/priority.html (accessed on 3 March 2021).
4. Chen, J.-Z.; Tao, X.-C.; Xu, J.; Zhang, T.; Liu, Z.-L. Biosorption of lead, cadmium and mercury by immobilized Microcystis aeruginosa in a column. *Process Biochem.* **2005**, *40*, 3675–3679. [CrossRef]
5. Dublis, S.; Shah, S.; Nand, S.; Anderes, E. Chapter 67-Anemias excluding cobalamin and folate deficiencies. In *Handbook of Clinical Neurology*; Biller, J., Ferro, J.M., Eds.; Elsevier: Amsterdam, The Netherlands, 2014; pp. 1005–1014. [CrossRef]
6. Khulbe, K.C.; Matsuura, T. Removal of heavy metals and pollutants by membrane adsorption techniques. *Appl. Water Sci.* **2018**, *8*, 19. [CrossRef]
7. Pasinszki, T.; Krebsz, M. Synthesis and Application of Zero-Valent Iron Nanoparticles in Water Treatment; Environmental Remediation; Catalysis, and Their Biological Effects. *Nanomaterials* **2020**, *10*, 917. [CrossRef] [PubMed]
8. Lu, H.-J.; Wang, J.-K.; Ferguson, S.; Wang, T.; Bao, Y.; Hao, H. Mechanism, synthesis and modification of nano zerovalent iron in water treatment. *Nanoscale* **2016**, *8*, 9962–9975. [CrossRef] [PubMed]
9. Wang, S.; Zhao, M.; Zhou, M.; Li, Y.C.; Wang, J.; Gao, B.; Sato, S.; Feng, K.; Yin, W.; Igalavithana, A.D.; et al. Biochar-supported nZVI (nZVI/BC) for contaminant removal from soil and water: A critical review. *J. Hazard. Mater.* **2019**, *373*, 820–834. [CrossRef]

10. Seipenbusch, M.; Rothenbacher, S.; Kirchhoff, M.; Schmid, H.-J.; Kasper, G.; Weber, A.P. Interparticle forces in silica nanoparticle agglomerates. *J. Nanoparticle Res.* **2010**, *12*, 2037–2044. [CrossRef]
11. Zhang, X.; Karunaratne, T.; Navarathna, C.; Zhang, J.; Pittman, C.U. Nanoscale zero-valent iron-decorated biochar for aqueous contaminant removal. In *Sustain. Biochar Water Wastewater Treat*; Mohan, D., Pittman, C.U., Mlsna, T.E., Eds.; Elsevier: Amsterdam, The Netherlands, 2022; pp. 611–641. [CrossRef]
12. Chen, W.; Pan, L.; Chen, L.; Wang, Q.; Yan, C. Dechlorination of hexachlorobenzene by nano zero-valent iron/activated carbon composite: Iron loading, kinetics and pathway. *RSC Adv.* **2014**, *4*, 46689–46696. [CrossRef]
13. Gil, A.; Amiri, M.J.; Abedi-Koupai, J.; Eslamian, S. Adsorption/reduction of Hg(II) and Pb(II) from aqueous solutions by using bone ash/nZVI composite: Effects of aging time, Fe loading quantity and co-existing ions. *Environ. Sci. Pollut. Res.* **2018**, *25*, 2814–2829. [CrossRef]
14. Zhang, X.; Navarathna, C.M.; Leng, W.; Karunaratne, T.; Thirumalai, R.V.K.G.; Kim, Y.; Pittman, C.U.; Mlsna, T.; Cai, Z.; Zhang, J. Lignin-based few-layered graphene-encapsulated iron nanoparticles for water remediation. *Chem. Eng. J.* **2021**, *417*, 129199. [CrossRef]
15. Aivalioti, M.; Pothoulaki, D.; Papoulias, P.; Gidarakos, E. Removal of BTEX, MTBE and TAME from aqueous solutions by adsorption onto raw and thermally treated lignite. *J. Hazard. Mater.* **2012**, *207–208*, 136–146. [CrossRef]
16. He, Q.; Ruan, P.; Miao, Z.; Wan, K.; Gao, M.; Li, X.; Huang, S. Adsorption of direct yellow brown D3G from aqueous solution using loaded modified low-cost lignite: Performance and mechanism. *Environ. Technol.* **2019**, *42*, 1642–1651. [CrossRef]
17. Samaraweera, H.; Sharp, A.; Edwards, J.; Pittman, C.U., Jr.; Zhang, X.; Hassan, E.B.; Thirumalai, R.V.K.G.; Warren, S.; Reid, C.; Mlsna, T. Lignite, thermally-modified and Ca/Mg-modified lignite for phosphate remediation. *Sci. Total Environ.* **2021**, *773*, 145631. [CrossRef] [PubMed]
18. Zhang, R.; Wang, B.; Ma, H. Studies on Chromium (VI) adsorption on sulfonated lignite. *Desalination* **2010**, *255*, 61–66. [CrossRef]
19. Qi, Y.; Hoadley, A.F.A.; Chaffee, A.L.; Garnier, G. Characterisation of lignite as an industrial adsorbent. *Fuel* **2011**, *90*, 1567–1574. [CrossRef]
20. Samaraweera, H.; Edwards, J.; Reid, C.; Perera, S.S.; Thirumalai, R.V.K.G.; Pittman, C.U., Jr.; Mlsna, T. Pyrolyzed Ca-impregnated lignite for aqueous phosphate removal: Batch and column studies. *J. Environ. Chem. Eng.* **2021**, *9*, 106077. [CrossRef]
21. Zhang, W.; Jiang, S.; Wang, K.; Wang, L.; Xu, Y.; Wu, Z.; Shao, H.; Wang, Y.; Miao, M. Thermogravimetric Dynamics and FTIR Analysis on Oxidation Properties of Low-Rank Coal at Low and Moderate Temperatures. *Int. J. Coal Prep. Util.* **2015**, *35*, 39–50. [CrossRef]
22. Milicevic, S.; Boljanac, T.; Martinovic, S.; Vlahovic, M.; Milosevic, V.; Babic, B. Removal of copper from aqueous solutions by low cost adsorbent-Kolubara lignite. *Fuel Process. Technol.* **2012**, *95*, 1–7. [CrossRef]
23. Di, J.; Ruan, Z.; Zhang, S.; Dong, Y.; Fu, S.; Li, H.; Jiang, G. Adsorption behaviors and mechanisms of Cu^{2+}, Zn^{2+} and Pb^{2+} by magnetically modified lignite. *Sci. Rep.* **2022**, *12*, 1394. [CrossRef]
24. Mehrabi, N.; Masud, A.; Afolabi, M.; Hwang, J.; Calderon Ortiz, G.A.; Aich, N. Magnetic graphene oxide-nano zero valent iron (GO–nZVI) nanohybrids synthesized using biocompatible cross-linkers for methylene blue removal. *RSC Adv.* **2019**, *9*, 963–973. [CrossRef] [PubMed]
25. Xing, M.; Wang, J. Nanoscaled zero valent iron/graphene composite as an efficient adsorbent for Co(II) removal from aqueous solution. *J. Colloid Interface Sci.* **2016**, *474*, 119–128. [CrossRef] [PubMed]
26. Sobhanardakani, S.; Jafari, A.; Zandipak, R.; Meidanchi, A. Removal of heavy metal (Hg(II) and Cr(VI)) ions from aqueous solutions using Fe_2O_3@SiO_2 thin films as a novel adsorbent. *Process. Saf. Environ. Prot.* **2018**, *120*, 348–357. [CrossRef]
27. Zhang, X.; Yan, Q.; Li, J.; Zhang, J.; Cai, Z. Effects of Physical and Chemical States of Iron-Based Catalysts on Formation of Carbon-Encapsulated Iron Nanoparticles from Kraft Lignin. *Materials* **2018**, *11*, 139. [CrossRef] [PubMed]
28. Zhang, X.; Yan, Q.; Hassan, E.B.; Li, J.; Cai, Z.; Zhang, J. Temperature effects on formation of carbon-based nanomaterials from kraft lignin. *Mater. Lett.* **2017**, *203*, 42–45. [CrossRef]
29. Zhang, X.; Yan, Q.; Li, J.; Chu, I.-W.; Toghiani, H.; Cai, Z.; Zhang, J. Carbon-Based Nanomaterials from Biopolymer Lignin via Catalytic Thermal Treatment at 700 to 1000 °C. *Polymers* **2018**, *10*, 183. [CrossRef]
30. Zhang, X. Synthesis and Characterization of Carbon-Based Nanomaterials from Lignin-ProQuest. 2016. Available online: https://www.proquest.com/docview/1858816366/abstract/9BE7891B9F3543B6PQ/1 (accessed on 17 January 2022).
31. Yan, Q.; Li, J.; Zhang, X.; Zhang, J.; Cai, Z. Mass production of graphene materials from solid carbon sources using a molecular cracking and welding method. *J. Mater. Chem. A* **2019**, *7*, 13978–13985. [CrossRef]
32. Yan, Q.; Li, J.; Zhang, X.; Zhang, J.; Cai, Z. In situ formation of graphene-encapsulated iron nanoparticles in carbon frames through catalytic graphitization of kraft lignin. *Nanomater. Nanotechnol.* **2018**, *8*, 1847980418818955. [CrossRef]
33. Yan, Q.; Li, J.; Zhang, X.; Zhang, J.; Cai, Z. Synthetic Bio-Graphene Based Nanomaterials through Different Iron Catalysts. *Nanomaterials* **2018**, *8*, 840. [CrossRef]
34. Zhou, Y.; Gao, B.; Zimmerman, A.R.; Chen, H.; Zhang, M.; Cao, X. Biochar-supported zerovalent iron for removal of various contaminants from aqueous solutions. *Bioresour. Technol.* **2014**, *152*, 538–542. [CrossRef]
35. Ling, L.; Huang, X.-Y.; Zhang, W.-X. Enrichment of Precious Metals from Wastewater with Core–Shell Nanoparticles of Iron. *Adv. Mater.* **2018**, *30*, 1705703. [CrossRef] [PubMed]
36. Tang, C.; Ling, L.; Zhang, W. Pb(II) deposition-reduction-growth onto iron nanoparticles induced by graphitic carbon nitride. *Chem. Eng. J.* **2020**, *387*, 124088. [CrossRef]

37. Samaraweera, H.; Pittman, C.U.; Thirumalai, R.V.K.G.; Hassan, E.B.; Perez, F.; Mlsna, T. Characterization of graphene/pine wood biochar hybrids: Potential to remove aqueous Cu^{2+}. *Environ. Res.* **2021**, *192*, 110283. [CrossRef] [PubMed]
38. Wang, Y.; Shao, Q.; Huang, S.; Zhang, B.; Xu, C. High performance and simultaneous sequestration of Cr(VI) and Sb(III) by sulfidated zerovalent iron. *J. Clean. Prod.* **2018**, *191*, 436–444. [CrossRef]
39. Du, Y.; Dai, M.; Cao, J.; Peng, C. Fabrication of a low-cost adsorbent supported zero-valent iron by using red mud for removing Pb(II) and Cr(VI) from aqueous solutions. *RSC Adv.* **2019**, *9*, 33486–33496. [CrossRef]
40. Pfeifer, A.; Škerget, M. A review: A comparison of different adsorbents for removal of Cr (VI), Cd (II) and Ni (II), Turk. *J. Chem.* **2020**, *44*, 859–883. [CrossRef]
41. Zhu, L.; Tong, L.; Zhao, N.; Li, J.; Lv, Y. Coupling interaction between porous biochar and nano zero valent iron/nano α-hydroxyl iron oxide improves the remediation efficiency of cadmium in aqueous solution. *Chemosphere* **2019**, *219*, 493–503. [CrossRef]
42. Zhang, X.; Yan, L.; Liu, J.; Zhang, Z.; Tan, C. Removal of Different Kinds of Heavy Metals by Novel PPG-nZVI Beads and Their Application in Simulated Stormwater Infiltration Facility. *Appl. Sci.* **2019**, *9*, 4213. [CrossRef]
43. O'Carroll, D.; Sleep, B.; Krol, M.; Boparai, H.; Kocur, C. Nanoscale zero valent iron and bimetallic particles for contaminated site remediation. *Adv. Water Resour.* **2013**, *51*, 104–122. [CrossRef]
44. Li, S.; Yang, F.; Li, J.; Cheng, K. Porous biochar-nanoscale zero-valent iron composites: Synthesis, characterization and application for lead ion removal. *Sci. Total Environ.* **2020**, *746*, 141037. [CrossRef]
45. Panayotova, M.; Velikov, B. Influence of Zeolite Transformation in a Homoionic Form on the Removal of Some Heavy Metal Ions from Wastewater. *J. Environ. Sci. Health Part A* **2003**, *38*, 545–554. [CrossRef] [PubMed]
46. Nieva, A.; Doma, B.; Chao, H.; Leng, L.S. Biosorption of Pb^{2+} and Cu^{2+} in aqueous solutions using agricultural wastes. *EPJ Web Conf.* **2017**, *162*, 01082. [CrossRef]
47. Wang, T.; Liu, W.; Xiong, L.; Xu, N.; Ni, J. Influence of pH, ionic strength and humic acid on competitive adsorption of Pb(II), Cd(II) and Cr(III) onto titanate nanotubes. *Chem. Eng. J.* **2013**, *215–216*, 366–374. [CrossRef]
48. Xiao, S.; Ma, H.; Shen, M.; Wang, S.; Huang, Q.; Shi, X. Excellent copper(II) removal using zero-valent iron nanoparticle-immobilized hybrid electrospun polymer nanofibrous mats. *Colloids Surf. Physicochem. Eng. Asp.* **2011**, *381*, 48–54. [CrossRef]
49. Cheng, P.; Hu, Y.H. Dubinin-Astakhov model for acetylene adsorption on metal-organic frameworks. *Appl. Surf. Sci.* **2016**, *377*, 349–354. [CrossRef]
50. Ho, Y.S.; McKay, G. Pseudo-second order model for sorption processes. *Process Biochem.* **1999**, *34*, 451–465. [CrossRef]
51. Toor, M.; Jin, B. Adsorption characteristics, isotherm, kinetics, and diffusion of modified natural bentonite for removing diazo dye. *Chem. Eng. J.* **2012**, *187*, 79–88. [CrossRef]
52. Voogd, P.; Scholten, J.J.F.; van Bekkum, H. Use of the t-plot—De Boer method in pore volume determinations of ZSM-5 type zeolites. *Colloids Surf.* **1991**, *55*, 163–171. [CrossRef]